IEEE Photonics Journal
An IEEE Photonics Society Publication

Open Access

High Figure of Merit Fano Resonance in 2-D Defect-Free Pillar Array Photonic Crystal for Refractive Index Sensing

Volume 8, Number 6, December 2016

Daquan Yang
Changhong Li
Chuan Wang
Yuefeng Ji
Qimin Quan

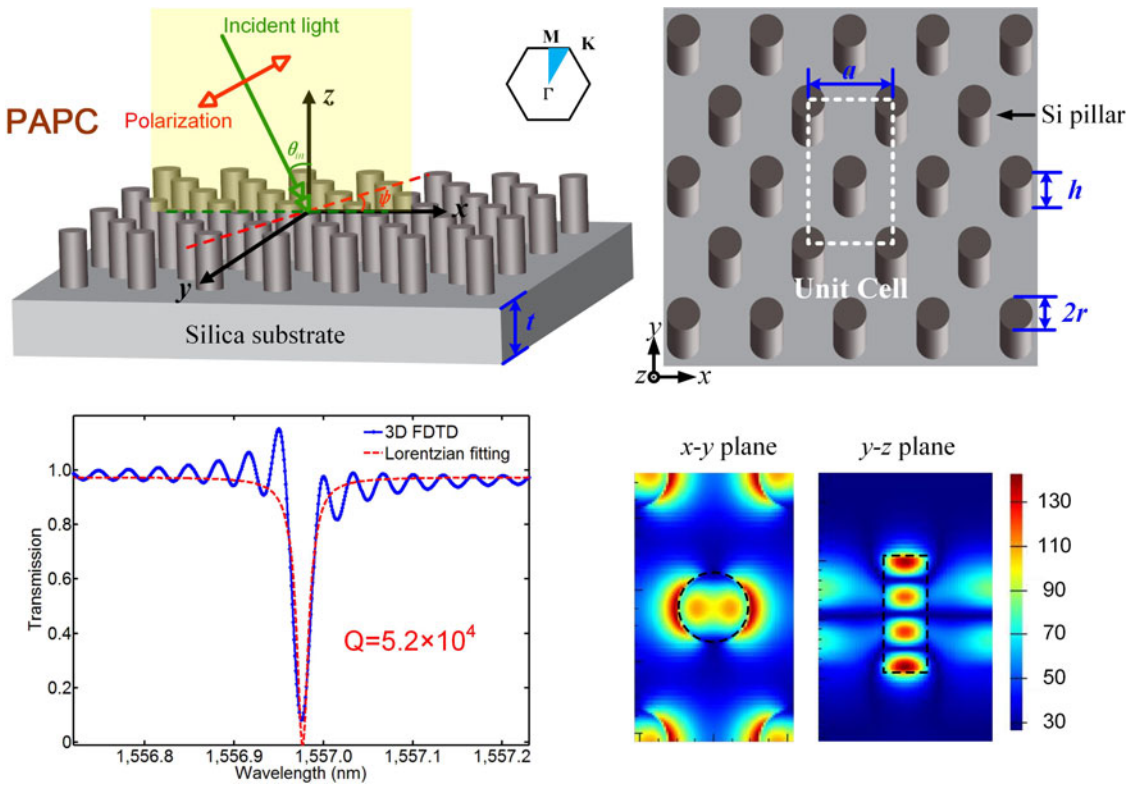

DOI: 10.1109/JPHOT.2016.2618851
1943-0655 © 2016 IEEE

High Figure of Merit Fano Resonance in 2-D Defect-Free Pillar Array Photonic Crystal for Refractive Index Sensing

Daquan Yang,[1] Changhong Li,[3] Chuan Wang,[1] Yuefeng Ji,[1,2] and Qimin Quan[4]

[1]State Key Laboratory of Information Photonics and Optical Communications, School of Information and Communication Engineering, Beijing University of Posts and Telecommunications, Beijing 100876, China
[2]Beijing Advanced Innovation Center for Future Internet Technology, Beijing University of Technology, Beijing 100124, China
[3]School of Electronic and Information Engineering, Qingdao University, Qingdao 266071, China
[4]Rowland Institute, Harvard University, Cambridge, MA 02142 USA

DOI:10.1109/JPHOT.2016.2618851

Manuscript received August 18, 2016; revised October 13, 2016; accepted October 14, 2016. Date of publication October 19, 2016; date of current version November 3, 2016. The work was supported in part by the Rowland Junior Fellowship Award at Rowland Institute, Harvard University; in part by the National Natural Science Foundation of China under Grant 61501053, Grant 61622103, Grant 61307050, and Grant 61372118; in part by the Fund of the State Key Laboratory of Information Photonics and Optical Communications (BUPT: IPOC2015ZC03); in part by the Fundamental Research Funds for the Central Universities (BUPT); and in part by the Funds of Beijing Advanced Innovation Center for Future Internet Technology of Beijing University of Technology (BJUT), China. Corresponding author: D. Yang (e-mail: yangdq5896@163.com)

Abstract: We present a simple and robust structure to realize Fano resonance for refractive index sensing applications. The Fano resonance with ultrahigh Q factors ($Q > 5.0 \times 10^4$) and high reflections (near 100%) is realized in a 2-D defect-free pillar array photonic crystal (PAPC) with optimized geometry (e.g., pillar array periodicity, height, and radius). We analyze its band structure, polarization, and transmission characteristics in detail with numerical methods (plane wave expansion and 3-D finite-difference time-domain (3-D-FDTD) simulations). The numerical results show that FOM $\sim 6.85 \times 10^3$ (FOM being the figure of merit) can be achieved, which is an order of magnitude improved over the previous work. In addition, the unique simplicity of this system in which a long-lifetime delocalized electromagnetic field exists and interacts with the surrounding media permits new opportunities for point-of-care applications. Furthermore, the proposed architecture makes the implementation of lab-on-a-chip refractive index sensing possible, which is enabled by integrating PAPC on the tip of an optical fiber.

Index Terms: Photonic crystals, sensors, silicon nanophotonics, fano resonance, theory and design, 3-D finite-difference time-domain (3-D FDTD).

1. Introduction

Over the past few decades, real-time and label-free detection has been extensively explored as a sensitive, compact, high-throughout, and portable technology in biomedical and chemical applications, ranging from the study of bio-molecular interactions to point-of-care diagnostics. Optical sensors have attracted increasing attention for lab-on-a-chip applications [1]–[3], such as

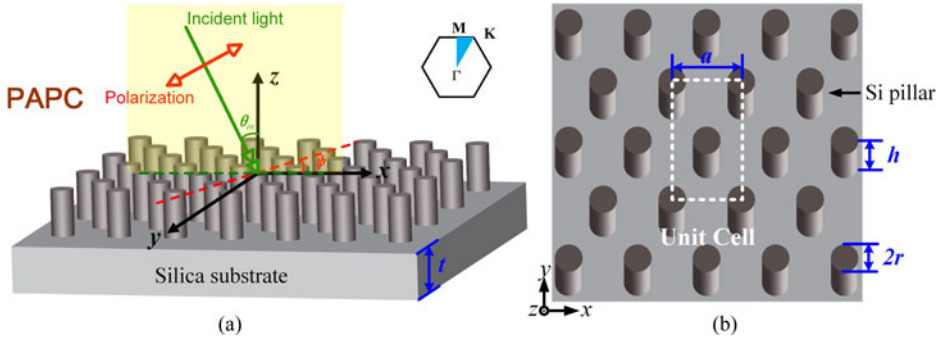

Fig. 1. (a) Schematics of the proposed pillar array photonic crystal (PAPC) structure. The incident angle (θ_{in}) and polarization angle (ψ) of the incident beam is defined as illustrated. The PAPC Brillouin zone symmetric points (Γ, M, and K) are shown in the inset. (b) Computation domain includes a single crystal unit cell (the white dashed line region), where a represents the periodicity, h and r are the pillar height and radius, and t is the thickness of the silica substrate. Here, $n_{si} = 3.46$, $n_{sio2} = 1.45$, and the background is air ($n_{air} = 1.0$). Excitation is a normally incident plane wave (along the $-z$-direction).

whispering-gallery micro-resonators (WGM) [4]–[9], ring resonators (RR) [10]–[15], surface plasmon resonance (SPR) devices [16]–[23], Mach-Zehnder interferometers (MZI) [24]–[27], and photonic crystals (PC) [28]–[49]. Among these approaches, PCs offer strong light confinement and enhanced light-matter interaction at the sub-micron scale, and thus has great potential in the development of ultra-compact integrated sensor arrays. However, coupling light to the sensors on chip requires high accuracy alignment and is becoming a limitation for point-of-care applications. Meanwhile, recent proposals for lab-on-a-tip architectures [50] could be an alternative strategy to lab-on-a-chip approaches. Integrating photonic crystal cavities on an optical fiber has been explored [51]–[53]. However, the defect-based photonic crystal cavities require fine device alignment to the fiber. To reduce the complexity in device fabrication and measurement, we propose to use Fano resonances in defect-free photonic crystals. Over the past years, Fano resonances have been observed in a wide variety of nanophotonic structures [54]–[56] and have been used for diodes [57], filters [58]–[60], spectroscopic imaging [61], modulators [62] and all-optical switching [63]–[66]. Fano resonances with sharp spectral features have been achieved in SPR [67]–[70] and PC [71]–[79] structures, which were used for biochemical sensing [67]–[75].

We propose a pillar array photonic crystal (PAPC) comprised of a triangular lattice of silicon pillars ($n_{si} = 3.46$) on a silica substrate ($n_{sio2} = 1.45$). With the 3-D finite-difference-time-domain (3-D-FDTD) method, we investigate the spectral dependence of Fano resonances on pillar array periodicity (a), pillar height (h), radius (r), and light incident angle (θ_{in}). From band diagrams, we also explain the origin of the Fano resonances. We demonstrate that high Q-factors of 5.2×10^4 can be obtained at telecom wavelength range (~1500 nm) with nearly 100% reflections. Furthermore, the numerical results show that an order of magnitude improvement of FoM (6.85×10^3) over the previous work [69]–[71] can be achieved.

2. Pillar Array Photonic Crystal (PAPC) With High Q Fano Resonance

The structure under study is schematically depicted in Fig. 1. It consists of a triangular lattice of silicon pillars ($n_{si} = 3.46$) on a silica substrate ($n_{sio2} = 1.45$). The thickness (t) of the silica substrate is 2 μm (Fig. 1). A PAPC may be entirely described by a unit cell with a periodicity, a, silicon pillar radius, r, and silicon pillar height, h, shown in Fig. 1(b). The computation domain includes a single unit cell, shown as the white dashed line region in Fig. 1(b). On the top and bottom surfaces perpendicular to the z-direction, we impose the Perfectly Matched Layer (PML) absorbing boundary conditions. For the remaining four surfaces, Bloch periodic boundary conditions are used in x- and y-axis. The incident source is a plane wave placed at a plane perpendicular to the z-direction,

and the light propagates along the -*z*-direction. During the simulation, the 3-D-FDTD algorithm (Lumerical Solutions Inc., Canada) is adopted for full vectorial electromagnetic calculations. In the simulation, the numerical calculations are performed with extremely well convergence conditions under different mesh sizes. Additionally, in order to improve accuracy of the simulation results, a 0.01 nm grid size is adopted. The computational domain encloses a single unit cell of the crystal.

The physical origin of the Fano resonances in PCs lies in the coupling between the guided modes above the light-line and the external plane waves [80], [81]. So far, extensive theoretical and experimental work for Fano resonances in the PCs platforms, such as PCs slabs and PCs cavities, have been demonstrated. In most cases, the line shapes for these Fano resonances are asymmetric. Thus, to clearly demonstrate the transmission spectrum of Fano resonance in PAPC, we next fit our 3D-FDTD simulation results with the well-known Fano line shape given below [55], [57], [81]–[84]:

$$T(\omega) = A_0 + T_0 \frac{[f + 2(\omega - \omega_0)/\Delta]^2}{1 + [2(\omega - \omega_0)/\Delta]^2} \tag{1}$$

where A_0 and T_0 are constant factors, ω_0 is the Fano resonant frequency, and Δ is the resonance line width. According to Fano's original work, the dimensionless parameter f describes the ratio between resonant and non-resonant transition amplitudes in the scattering process. It accounts for the lineshape asymmetry and can assume either positive or negative values. By looking at (1), according to the value of the asymmetry parameter f, which describes the ratio between resonant and non-resonant transition amplitudes, the Fano line shapes can be categorized into following three cases: i) In usual cases for $|f|$ values of the order of unity ($|f| \geq 1$), i.e., when resonant and direct scattering amplitudes are comparable with each other, a strongly asymmetric resonance is observed; ii) when $|f|$ values is large, meaning that resonant scattering dominates over direct scattering, the observed lineshape tends toward a symmetric Lorentzian; iii) finally, for small $|f|$ values ($|f| < 1$), i.e., when resonant scattering is small compared to direct scattering, the Fano profile takes the form of a reversed Lorentzian [82], [83]. Thus, the analysis of the resonant line shape allows us to determine the quality factor (Q) is defined as [81]

$$Q = \frac{\omega_0}{\Delta}. \tag{2}$$

The transmission property, therefore, is determined by the interference between the direct and indirect pathways.

Herein, as shown in Fig. 1(a), the incident beam is restricted to be within the plane in parallel with the *x*-*z* plane, i.e., kept at the azimuthal angle is zero (angle from the positive *x*-axis to the orthogonal projection of the incident beam in the *x*-*y* plane). In this case, the incident beam plane corresponds the Γ-M direction in the κ-space. Thus, the incidence direction can be only specified by the incidence angle θ_{in} (namely colatitude angle, angle from the normal direction). The incidence polarization angle (ψ) is defined as the angle from the positive *x*-axis to the projection of polarization direction in the *x*-*y* plane, i.e., $\psi = 0^\circ$ for Ex-polarized beam and $\psi = 90^\circ$ for Ey-polarized beam. These angles are schematically shown in Fig. 1(a) in detail. We investigate the case that silicon pillars ($n_{si} = 3.46$) form a triangular lattice on the silica substrate ($n_{sio2} = 1.45$). The top is air ($n_{air} = 1.0$). We perform optical characterization of the PAPC by using a plane wave source at different incident angles (θ_{in}) from $\theta_{in} = 0^\circ$ to $\theta_{in} = 10^\circ$, with the periodicity $a = 870$ nm, pillar radius $r = 0.2a$ and height $h = 1.12\ \mu m$ fixed. Based on 3-D-FDTD method, the simulated transmission spectra for different incident angles (θ_{in}) are shown in Fig. 2(a) and (b) for the different Ex- and Ey-polarized incident beams, respectively. As seen from Fig. 2(a) and (b), note that the simulated transmission spectra of PAPC do not have the varying Fabry-Perot curves due to decoupling of the dielectric media. Instead, we observe a good transmission with nearly symmetric sharp reflective peaks (e.g. λ_{1x}, λ_{2x}, λ_{1y}, λ_{2y}, and λ_{3y}) at telecom wavelength range ($\sim$1500 nm). Here, the simulated results agree well with [85].

Furthermore, we use plane wave expansion (PWE) to solve the band diagram (see Fig. 2(c)) in order to identify the origin of each Fano resonance. Fig. 2(d) is the zoom-in of the black-dashed

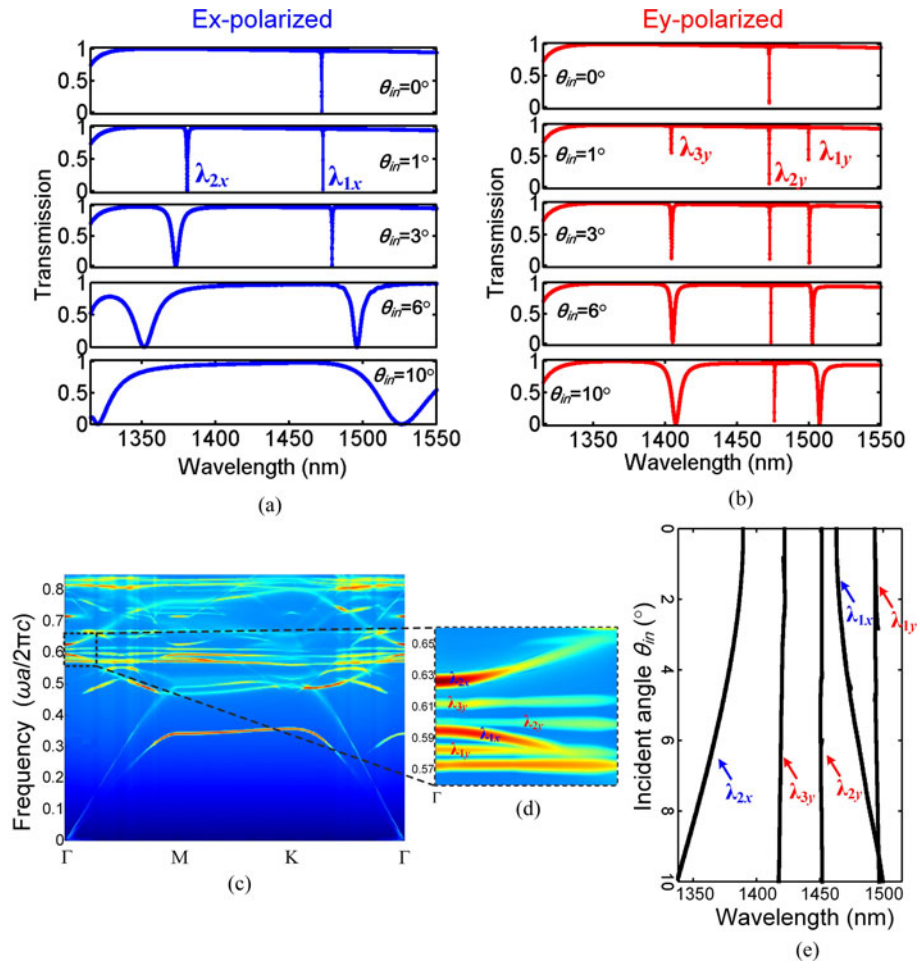

Fig. 2. The 3-D-FDTD simulated transmission spectra of PAPC for various incidence angles from $\theta_{in} = 0^\circ$ to $\theta_{in} = 10^\circ$ under different polarization conditions. (a) Γ-M direction with Ex-polarization. (b) Γ-M direction with Ey-polarization. (c) Band diagram of the triangular lattice PAPC obtained from PWE simulation, where the periodicity $a = 870$ nm, radius (r), and height (h) of *Si*-pillars are $r = 0.2a$ and $h = 1.12$ μm, respectively. The light beam is at normal incidence. (d) Zoom in of black-dashed line area in band diagram (c). (e) Convert κ_x to the incidence angle (θ_{in}) with the wavelength range between 1350 nm to 1500 nm.

line area in band diagram (see Fig. 2(c)). Fig. 2(e) converted κ_x in band diagram to the incidence angle (θ_{in}) with the wavelength range between 1350 nm to 1500 nm, $\kappa_x = (\omega/c) \cdot \sin(\theta_{in})$, where the ω represents frequency. All of the resonant modes obtained in the transmission spectra under different polarized light (λ_{1x}, λ_{2x}, λ_{1y}, λ_{2y}, and λ_{3y} marked in Fig. 2(a) and (b), respectively) were identified in the band diagram (see Fig. 2(d)). When the incident angle (θ_{in}) increases from 0° to 10°, Fano resonant modes λ_{1x} and λ_{2x} shift towards longer wavelengths (red-shift) and shorter wavelengths (blue-shift), respectively, which agrees well with the band dispersion (λ_{1x} and λ_{2x}) in Fig. 2(d). Fano resonant mode λ_{2y} remains almost unchanged over the range of incident angles (θ_{in}) from 0° to 10°, which also agrees well with the band dispersion in Fig. 2(d).

Fig. 3 depicts the Q-factors of Fano resonant modes λ_{1x} and λ_{2y} as a function of the incident angle. As the incident angle changes from $\theta_{in} = 0^\circ$ to $\theta_{in} = 10^\circ$, Fano resonant mode λ_{2y}, displays little variations in Q-factors ($> 10^4$) while the mode λ_{1x} displays a large variation. When the incident angle $\theta_{in} = 0^\circ$ (normal incidence), Q-factors of both Fano resonant modes λ_{1x} and λ_{2y} are as high as 1.26×10^4 and 1.13×10^4, respectively. In the following sections, we investigate and optimize

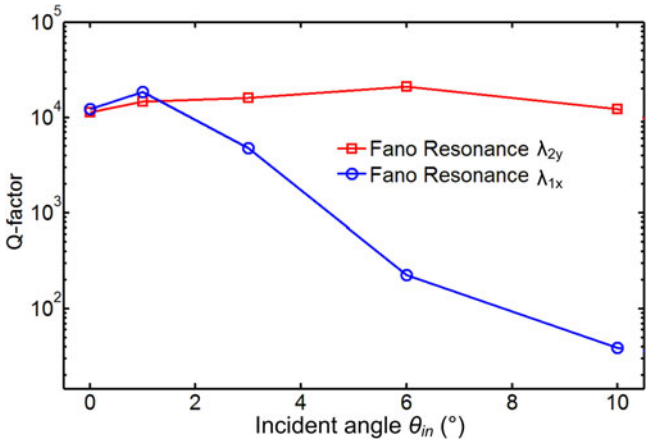

Fig. 3. Simulation results of Q-factors of the Fano resonant modes λ_{1x} and λ_{2y} in Fig. 2, with respect to the incident angle θ_{in}.

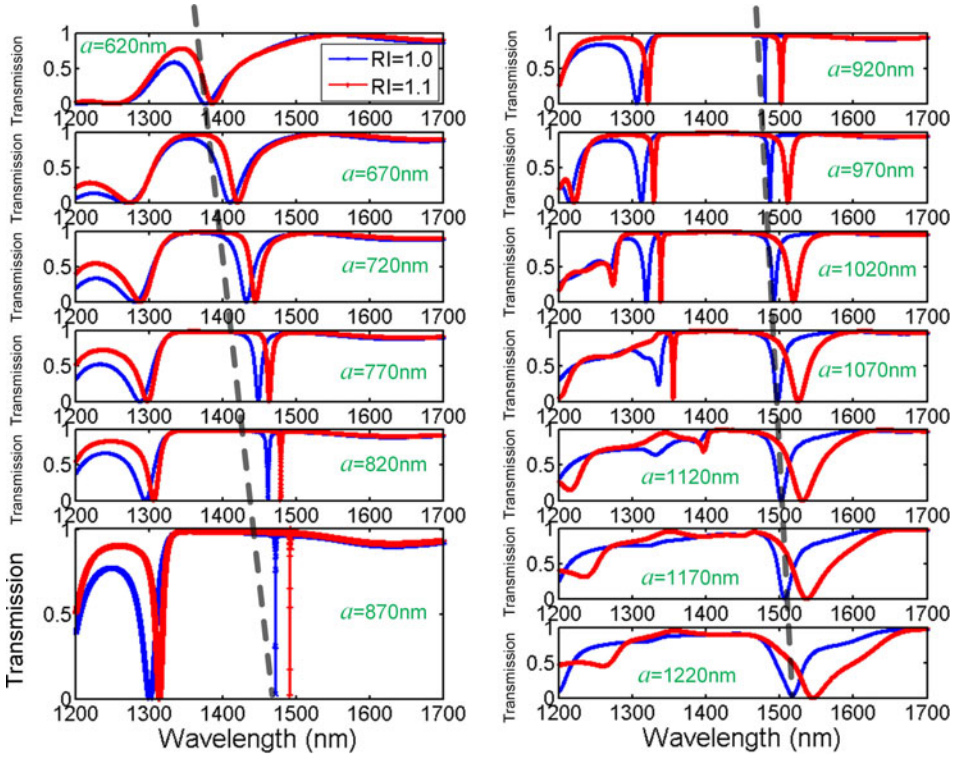

Fig. 4. Simulated transmission spectra of the Ex-polarized normal incident plane wave on PAPC for various periodicities a (620 nm to 1220 nm). Silicon pillar height $h = 1120$ nm and pillar radius $r = 174$ nm are fixed. Blue and red curves are, respectively, for the background refractive index RI $= 1.0$ and RI $= 1.1$. The dashed black line traces the shifts of the Fano resonant modes.

the spectral properties of the Fano resonances as of pillar array periodicity (a), pillar height (h), pillar radius (r), and light beam polarizations (ψ).

3. Optimization

In this section, we consider the case when the light beam has an incidence angle $\theta_{in} = 0^\circ$ and Ex-polarization ($\psi = 0^\circ$). We investigate the effects of the periodicity (a), pillar height (h), and radius

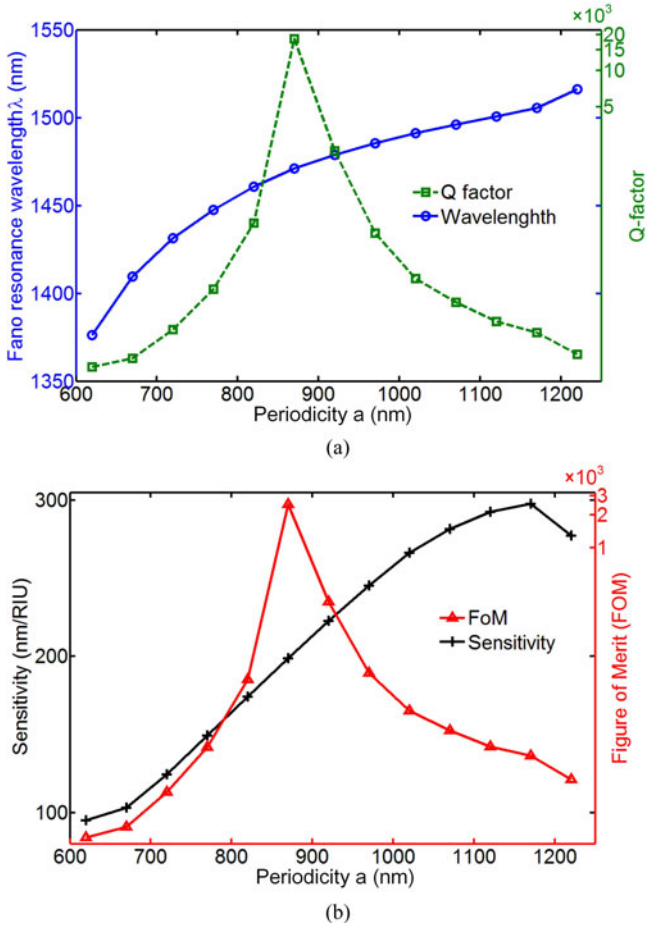

Fig. 5. Influence of periodicities on (a) resonant wavelength and Q-factors and (b) sensitivities and FoMs of the Fano resonances, while other parameters of silicon pillar height $h = 1120$ nm and pillar radius $r = 174$ nm are fixed.

(r) on the resonant wavelength (λ_{res}), Q-factors, refractive index sensitivities (S), and figure of merit (FoM). Based on the optimal parameters, we further discuss its polarizations (ψ) dependence.

We introduce a bulk refractive index (RI) sensitivity, S (in nm/RIU), and relate it to the resonance shift $\Delta\lambda$ due to a change in refractive index Δn of the medium

$$S = \frac{\Delta\lambda}{\Delta n}. \tag{3}$$

The FoM is defined as [86]

$$FoM = \frac{S \times Q}{\lambda_{res}} \tag{4}$$

where λ_{res} is the resonant wavelength, and Q is the quality factor.

3.1 The Dependence of Periodicity (a)

We start by investigating the effect of periodicity (a) on the Fano resonances in PAPC. Fig. 4 shows the transmission spectra at normal incidence for different pillar array periodicities (from $a = 620$ nm to $a = 1220$ nm) when other parameters are fixed (silicon pillar height $h = 1120$ nm, radius $r = 174$ nm). The positions of all the Fano resonances increase in wavelength as the periodicity increased. The Q

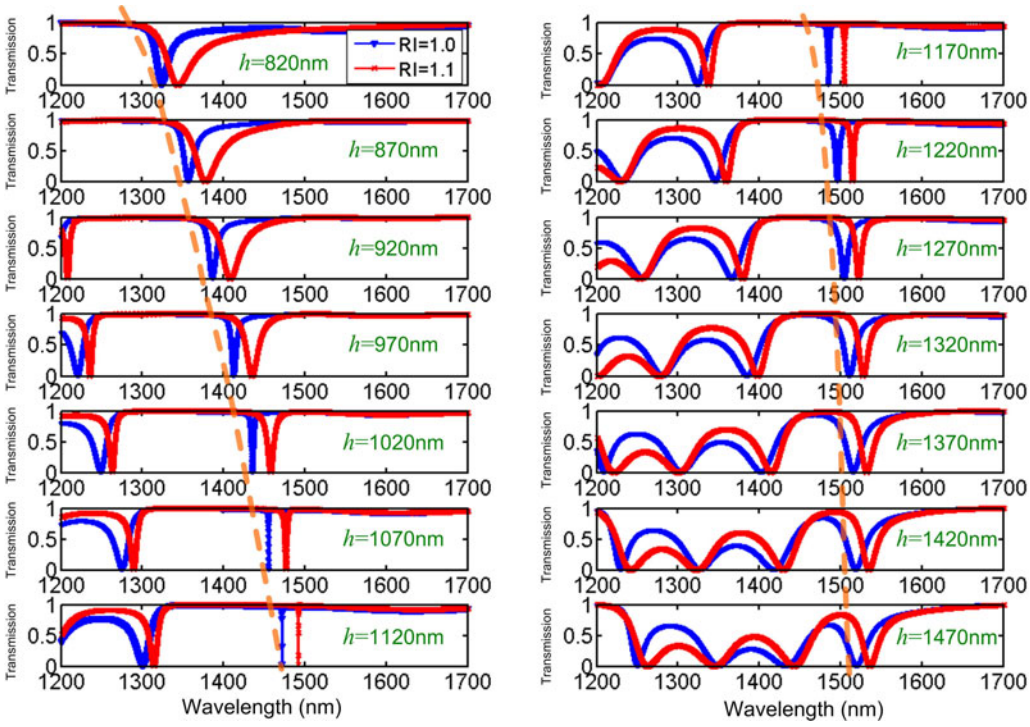

Fig. 6. Simulated transmission spectra of the Fano resonance at normal incidence for various values of the silicon pillar heights h (820 nm to 1470 nm). Periodicity $a = 870$ nm, and pillar radius $r = 0.2a$ are fixed. Blue and red curves are, respectively, for the RI = 1.0 and 1.1 background refractive indices. The dashed orange line traces the resonance shift of the Fano resonances.

factor maximizes at around 1.85×10^4 with near-to-100% reflectivity when periodicity $a = 870$ nm, as shown in Fig. 5(a). Moreover, as shown in Fig. 4, the Fano resonance displays little variation in line-widths and spectral positions over the range of periodicity from $a = 820$ nm to $a = 970$ nm. Therefore, the whole structure is immune to fabrication imperfections.

Next, we optimize the periodicity of PAPC to achieve high FoM. Fig. 5(b) shows the RI sensitivities and the FoMs varying as a function of the periodicity increased from $a = 620$ nm to $a = 1220$ nm. Here, the sensitivity is defined as (3), i.e., the resonant wavelength shift ($\Delta\lambda$) induced by the change of refractive index ($\Delta n = 0.1$, as the refractive index changed from RI = 1.0 to RI = 1.1). As seen in Fig. 5(b), the sensitivity increases as the periodicity (a) increases in general. When the periodicity (a) is 1170 nm, the sensitivity reaches as high as 300 nm/RIU. In addition, when the periodicity is 870 nm, the FoM reaches the maximum value of 2.5×10^3, which is more than an order of magnitude higher than the previous work [69]–[71].

3.2 The Dependence of Silicon Pillar Height (h)

Second, we consider the dependence of Fano resonances on silicon pillar height (h) of PAPC. Fig. 6 shows the transmission spectra at normal incidence for PAPC with different pillar heights (h) from $h = 820$ nm to $h = 1470$ nm. The periodicity (a) and radius (r) of pillars are kept fixed at $a = 870$ nm and a ratio of $r/a = 0.20$. In Fig. 6, when the *Si*-pillar height increases, a stronger Fano resonance occurs, leading to a larger number of Fano resonant modes inside PAPC. As the pillar height increases, the resonance shifts towards a longer wavelength (see Fig. 7(a)), which agrees well with the report displayed in [75], [87]. The Q of the Fano resonant mode reaches 1.85×10^4 when the pillar height $h = 1120$ nm, as shown in Fig. 7(a). Fig. 7(b) shows the RI sensitivities and

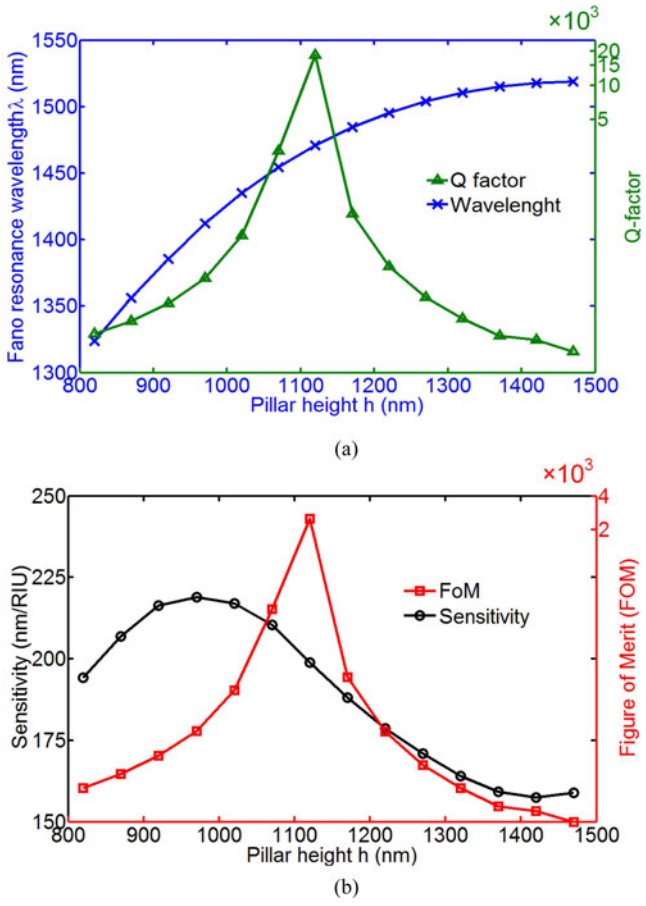

Fig. 7. Influence of the pillar height h on (a) resonant wavelengths and Q-factors and (b) sensitivities and FoMs of the Fano resonances, while other structure parameters are fixed (periodicity $a = 870$ nm and pillar radius $r = 0.2a$).

the FoMs varying as a function of the pillar height increases from $h = 820$ nm to $h = 1470$ nm. As seen, when the pillar height (h) is 1120 nm, the FoM reaches the maximum value of 2.5×10^3.

3.3 The Dependence of Silicon Pillar Radius (r)

Third, we study the dependence of Fano resonance on the pillar radius. We plot the transmission spectra with radius (r) varying from 140 nm ($0.16a$) to 330 nm ($0.38a$) in Fig. 8. The other parameters are chosen at periodicity $a = 870$ nm and pillar height $h = 1120$ nm. As the pillar radius increases, the Fano resonance shifts to longer wavelength, as shown in Fig. 8. Additionally, there is only one Fano resonance in the wavelength range greater than 500 nm (see Fig. 8), which is ideal for applications such as tunable filters, optical switch, and sensors.

Fig. 9(a) shows that high Q Fano resonance shifts towards longer wavelength, while Q is maximized ($\sim 5.2 \times 10^4$) at 1556.97 nm when pillar radius $r = 190$ nm. The zoom-in spectrum is shown in Fig. 9(c). Fig. 9(d) and (e) shows E-field distribution in the x-y plane and y-z plane at resonant wavelength (1556.97 nm) when Q reaches maximum. Next, we optimize the pillar radius (r) of PAPC to achieve the highest FoM. Fig. 9(b) shows the RI sensitivities (S) and the FoMs varying as a function of the pillar radius with other parameters (pillar array periodicity a and pillar height h) are kept fixed. When the pillar radius (r) is 190 nm, the FoM reaches the maximum value of

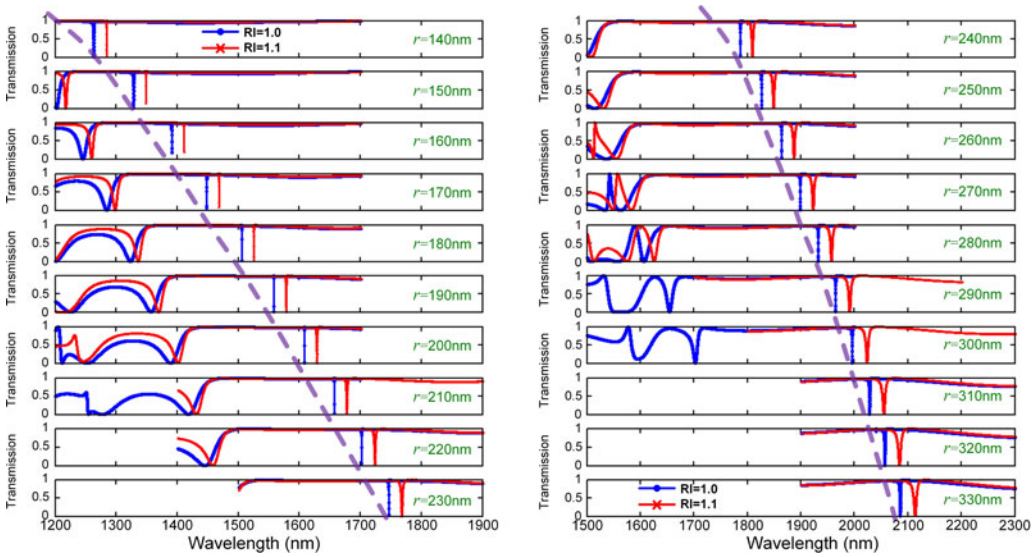

Fig. 8. Simulated transmission spectra at normal incidence for various values of the silicon pillar radii r (140 nm to 330 nm). Periodicity $a = 870$ nm and pillar height $h = 1120$ nm are kept fixed. Blue and red curves are calculated for RI = 1.0 and 1.1 cases, respectively. The dashed purple line traces the resonance shift of the high-Q Fano resonant mode.

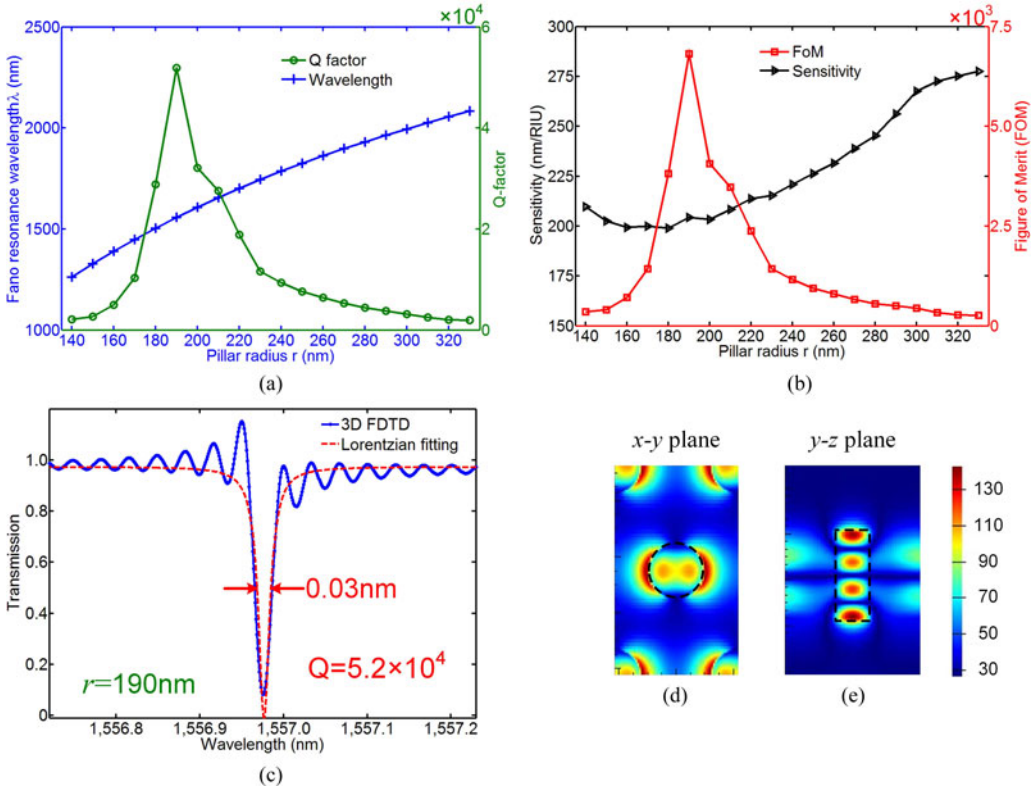

Fig. 9. Influence of the pillar radii r on (a) Fano resonant wavelengths and the corresponding Q-factors and (b) sensitivities and FoMs of Fano resonance, respectively, while other structure parameters are kept fixed ($a = 870$ nm and $h = 1120$ nm). (c) Zoom-in spectrum of the Fano resonance (pillar radius $r = 190$ nm) achieves high $Q = 5.2 \times 10^4$. Simulated E-field ($|E|$) distribution profiles in (d) x-y plane and (e) cross section y-z plane, respectively, at resonant wavelength (1556.97 nm) for $r = 190$ nm, $a = 870$ nm, and $h = 1120$ nm, representing the highest Q condition for this design.

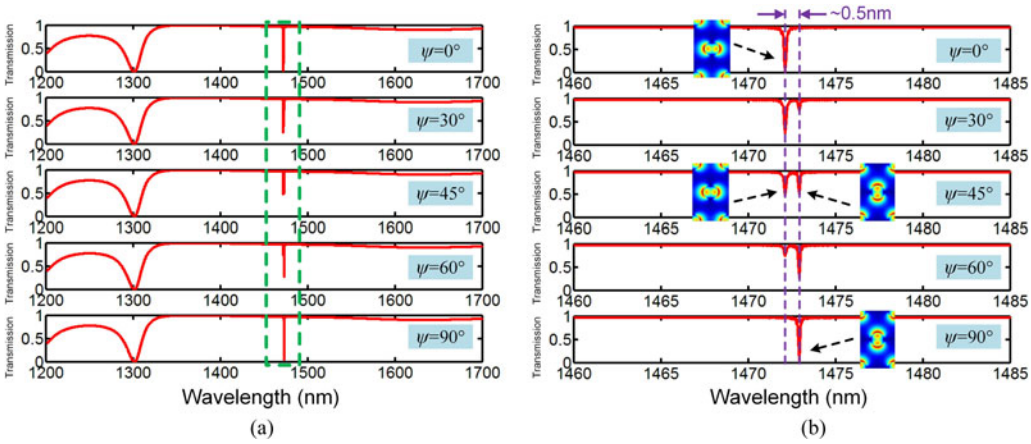

Fig. 10. (a) Transmission spectra of the incident light with different polarization at normal incidence (polarization angles $\psi = 0^\circ$, 30°, 45°, 60°, and 90°) with the periodicity $a = 870$ nm, pillar radius $r = 0.2a$, and height $h = 1120$ nm. (b) Zoom-in spectra of the dashed green line region in (a). Insets are 3-D-FDTD simulated E-field distribution profiles in x-y plane for different Fano resonant modes with different polarization angles.

6.85×10^3, more than an order of magnitude higher than the previous work [69]–[71]. Additionally, the calculated sensitivity as high as 205 nm/RIU can be obtained.

3.4 The Dependence of Light Beam Polarization Angle (ψ)

We consider Fano resonances at different incident polarization angles (ψ) at normal incidence, and choose the structure periodicity $a = 870$ nm, pillar radius $r = 0.2a$, and height $h = 1120$ nm. Fig. 10(a) shows a comparison of the transmission spectra for the polarization angles $\psi = 0^\circ$, 30°, 45°, 60°, and 90°. Fig. 10(b) displays the zoom-in spectra for the dashed green line region indicated in Fig. 10(a). As the polarization angles changed from $\psi = 0^\circ$ (x-polarized) to $\psi = 90^\circ$ (y-polarized), it is interesting to note that i) the Fano resonance lineshape always keep symmetrical; ii) compared with x-polarized, the transmission spectra for y-polarized incidence exhibiting wavelength a little shift ~0.5 nm is displayed; iii) for the other polarization angles, e.g., $\psi = 30^\circ$, $\psi = 45^\circ$, and $\psi = 60^\circ$, there are two transmission dips. And the amplitudes ratio between these two dip are changed for different polarization angles. However, the sum of the transmission is always unity, indicating that both polarizations are orthogonal and each has 100% transmission. Thus, PAPC can be used to detect incident angle polarization. The insets display the 3-D-FDTD simulated E-field distribution profiles in x-y plane for different Fano resonant modes with different polarization angles.

4. Application: Fano Resonant Refractive Index Sensor

Herein, based on the simulation results and discussion shown in Section 3, a summary to show the parameters for the optimized Fano resonant PAPC sensor are as follows: The proposed Fano resonant PAPC sensor structure is constructed by arranging a triangular lattice of silicon pillars ($n_{si} = 3.46$) on a silica substrate ($n_{sio2} = 1.45$). The thickness of the silica substrate is 2.0 μm (Fig. 1). The periodicity is $a = 870$ nm. The bulk radius and heights of Si-pillar are $r = 0.2a$, and $h = 1.12$ μm, respectively. And the background is air ($n_{air} = 1.0$). By using 3-D-FDTD method, Fig. 11(a) shows transmission spectrum of a normally incident Ex-polarized light excited along the z-direction with $\theta_{in} = 0^\circ$ and $\psi = 0^\circ$. As seen in Fig. 1, a high Q-factor Fano resonant mode (FRM) at 1470 nm with near 100% reflection is obtained. In order to investigate the RI sensitivity of the proposed Fano resonant PAPC sensor, various refractive indices of the media are tested, as displayed in Fig. 11(b). As seen in Fig. 11(b) and (c), it reveals that the Fano resonant wavelength shifts its resonance towards to longer wavelength (red-shift) when the RI values increased from RI = 1.0

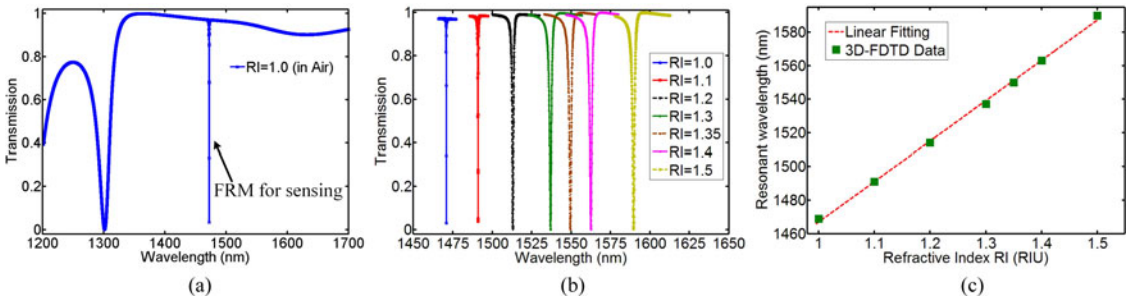

Fig. 11. (a) The 3-D-FDTD transmission spectrum of the Ex-polarized incident light at normal incidence ($\psi = 0^\circ$, $\theta_{in} = 0^\circ$) along the z-direction, with the optimized parameters of periodicity $a = 870$ nm, pillar radius $r = 0.2a$, and height $h = 1.12\ \mu m$. (b) Composed transmission spectra of the proposed Fano resonant PAPC sensor observed when the refractive index of surrounding media changed from RI = 1.0 to RI = 1.5. (c) Resonant wavelength shifts towards longer wavelengths (red-shift) as RI increases.

to RI = 1.5. Fig. 11(c) shows the shifts of Fano resonant wavelength as a function of the changed refractive index of the surrounding media of the sensor structure. As seen, the resonant wavelength shifts its resonance following a linear behavior when the RI values changed, and the correlation factors (R^2) is found to be >0.9998. Based on the simulation results displayed in Fig. 11, the bulk RI sensitivity of the proposed Fano resonant sensor can be calculated from the definition of $S = \Delta\lambda/\Delta\text{RI}$, where S is the bulk RI sensitivity, $\Delta\lambda$ is the resonant wavelength shift, and ΔRI is the surrounding RI change. Thus, the bulk RI sensitivities of 242 nm/RIU is observed.

5. Conclusion

In conclusion, we numerically investigated the spectral characteristics of Fano resonance in pillar array photonic crystal (PAPC) with triangular lattice. We first study the Fano resonance transmission spectra properties (e.g., resonant wavelength, Q-factors, RI sensitivities, and FoMs) and its dependence on the pillar array periodicity (a), pillar height (h), and radius (r). The simulation results show that the optimal Fano resonance has high Q-factor of 5.2×10^4 in air and FoM of 6.85×10^3, more than an order of magnitude higher than the previous work. Furthermore, angular and polarization dependent transmission properties of the Fano resonant PAPC are also investigated. Both Ex-polarized mode and Ey-polarized mode have high Q-factors, and they are spectrally separated by 0.5 nm. In addition, the proposed architecture is potentially an ideal platform for high performance remote sensing applications by integrating PAPC on the tip of an optical fiber.

Acknowledgment

The authors would like to thank Prof. M. Loncar at Harvard University for helpful comments.

References

[1] R. Daw and J. Finkelstein, "Lab on a chip," *Nature*, vol. 442, pp. 367–418, 2006.
[2] X. Fan *et al.*, "Sensitive optical biosensors for unlabeled targets: A review," *Anal. Chim. Acta*, vol. 620, pp. 8–26, 2008.
[3] H. K. Hunt and A. M. Armani, "Label-free biological and chemical sensors," *Nanoscale*, vol. 2, pp. 1544–1559, 2010.
[4] M. Foreman, J. Swaim, and F. Vollmer, "Whispering gallery mode sensors," *Adv. Opt. Photon.*, vol. 7, no. 2, pp. 168–240, 2015.
[5] B. Li, W. Clements, X. Yu, K. Shi, Q. Gong, and Y. Xiao, "Single nanoparticle detection using split-mode microcavity Raman lasers," in *Proc. Nat. Acad. Sci.*, vol. 111, no. 41, pp. 14657–14662, 2014.
[6] M. Baaske, M. Foreman, and F. Vollmer, "Single-molecule nucleic acid interactions monitored on a label-free microcavity biosensor platform," *Nature Nanotechnol.*, vol. 9, pp. 933–939, 2014.
[7] K. Khosla, J. Swaim, J. Knittel, and W. P. Bowen, "Yield enhancement in whispering gallery mode biosensors: Microfluidics and optical forces," *J. Modern Opt.*, vol. 61, pp. 415–418, 2014.

[8] L. He, S. K. Ozdemir, J. Zhu, W. Kim, and L. Yang, "Detecting single viruses and nanoparticles using whispering gallery microlasers," *Nature Nanotechnol.* vol. 6, no. 428–432, 2011.
[9] F. Vollmer and S. Arnold, "Whispering-gallery-mode biosensing: Label-free detection down to single molecules." *Nature Methods*, vol. 5, pp. 591–596, 2008.
[10] C. Smith, R. Shankar, M. Laderer, M. B. Frish, M. Loncar, and M. Allen, "Sensing nitrous oxide with QCL-coupled silicon-on-sapphire ring resonators," *Opt. Exp.*, vol. 23, no. 5, pp. 5491–5499, 2015.
[11] J. H. Wade and R. C. Bailey, "Refractive index-based detection of gradient elution liquid chromatography using chip-integrated microring resonator arrays," *Anal. Chem.*, vol. 86, pp. 913–919, 2014.
[12] M. Li, X. Wu, L. Liu, X. Fan, and L. Xu, "Self-referencing optofluidic ring resonator sensor for highly sensitive biomolecular detection,"*Anal. Chem.* vol. 85, no. 19, pp. 9328–9332, 2013.
[13] X. Fan and I. M. White, "Optofluidic microsystems for chemical and biological analysis," *Nature Photon.*, vol. 5, pp. 591–597, 2011.
[14] C. F. Carlborg *et al.*, "A packaged optical slot-waveguide ring resonator sensor array for multiplex label-free assays in labs-on-chips," *Lab Chip*, vol. 10, pp. 281–290, 2010.
[15] M. Iqbal *et al.*, "Label-free biosensor arrays based on silicon ring resonators and high-speed optical scanning instrumentation," *IEEEJ. Sel. Topics Quantum Electron.*, vol. 16, no. 3, pp. 654–661, May/Jun. 2010.
[16] Y. Liu, S. Chen, Q. Liu, J. Masson, and W. Peng, "Compact multi-channel surface plasmon resonance sensor for real-time multi-analyte biosensing," *Opt. Exp.*, vol. 23, no. 16, pp. 20540–20548, 2015.
[17] S. Zeng, D. Baillargeat, H. Hod, and K. Yong, "Nanomaterials enhanced surface plasmon resonance for biological and chemical sensing applications," *Chem. Soc. Rev*. vol. 43, pp. 3426–3452, 2014.
[18] H. Im *et al.*, "Label-free detection and molecular profiling of exosomes with a nano-plasmonic sensor," *Nature Biotechnol*. vol. 32, no. 5, pp. 490–495, 2014.
[19] P. He, L. Liu, W. Qiao, and S. Zhang, "Ultrasensitive detection of thrombin using surface plasmon resonance and quartz crystal microbalance sensors by aptamer-based rolling circle amplification and nanoparticle signal enhancement," *Chem. Commun.*, vol. 50, pp. 1481–1484, 2014.
[20] H. Sipova and J. Homola, "Surface plasmon resonance sensing of nucleic acids: A review," *Analytica Chimica Acta*, vol. 773, pp. 9–23, 2013.
[21] C. Huang, G. Yao, R. Liang, and J. Qiu, "Graphene oxide and dextran capped gold nanoparticles based surface plasmon resonance sensor for sensitive detection of concanavalin A," *Biosens. Bioelectron.*, vol. 50, pp. 305–310, 2013.
[22] P. Zijlstra, P. M. R. Paulo, and M. Orrit, "Optical detection of single non-absorbing molecules using the surface plasmon resonance of a gold nanorod," *Nature Nanotechnol.*, vol. 7, pp. 379–382, 2012.
[23] R. C. Jorgenson and S. S. Yee, "A fiber-optic chemical sensor based on surface plasmon resonance," *Sens. Actuators B, Chem.*, vol. 12, pp. 213–220, 1993.
[24] K. Misiakos *et al.*, "Broad-band Mach–Zehnder interferometers as high performance refractive index sensors: Theory and monolithic implementation," *Opt. Exp.*, vol. 22, no. 8, pp. 8856–870, 2014.
[25] J. Wo *et al.*, "Refractive index sensor using microfiber-based Mach–Zehnder interferometer," *Opt. Lett.*, vol. 37, no. 67–69, 2012
[26] A. Ymeti *et al.*, "Fast, ultrasensitive virus detection using a young interferometer sensor," *Nano Lett.*, vol. 7, no. 2, pp. 394–397, 2007.
[27] P. Hua, B. Luff, G. Quigley, J. Wilkinson, and K. Kawaguchi, "Integrated optical dual Mach–Zehnder interferometer sensor," *Sens. Actuators B, Chem.*, vol. 87, pp. 250–257, 2002.
[28] X. Zhang *et al.*, "On-chip integrated optofluidic complex refractive index sensing using silicon photonic crystal nanobeam cavities," *Opt. Lett.*, vol. 41, pp. 1197–1200, 2016.
[29] Y. Chen, W. S. Fegadolli, A. Scherer, and M. Li, "Nanobeam photonic crystal cavity based multifunctional gas-phase chemical sensor," in *Proc. Conf. Lasers Electro-Opt.*, 2014, paper SM3E.5.
[30] T. Lin, X. Zhang, G. Zhou, C. Siong, and J. Deng, "Design of an ultra-compact slotted photonic crystal nanobeam cavity for biosensing," *J. Opt. Soc. Amer. B*, vol. 32, 1788–1791, 2015.
[31] F. Liang and Q. Quan, "Detecting single gold nanoparticles (1.8 nm) with ultrahigh-Q airMode photonic crystal nanobeam cavities," *ACS Photon.*, vol. 2, pp. 1692–1697, 2015.
[32] P. Xu, K. Yao, J. Zheng, X. Guan, and Y. Shi, "Slotted photonic crystal nanobeam cavity with parabolic modulated width stack for refractive index sensing," *Opt. Exp.*, vol. 21, pp. 26908–26913, 2013.
[33] Q. Quan *et al.*, "Single particle detection in CMOS compatible photonic crystal nanobeam cavities," *Opt. Exp.*, vol. 21, no. 26, pp. 32225–32233, 2013.
[34] S. George, V. Chaudhery, Y. Tan, M. Lu, and B. T. Cunningham, "Sensitive detection of protein and miRNA Cancer biomarkers using silicon-based photonic crystals and a resonance coupling laser scanning platform," *Lab Chip*, vol. 13, pp. 4053–4064, 2013.
[35] C. Wang, Q. Quan, S. Kita, Y. Li, and M. Loncar, "Single-nanoparticle detection with slot-mode photonic crystal cavities," *Appl. Phys. Lett.*, vol. 106, 2015, Art. no. 261105.
[36] D. Yang, H. Tian, Y. Ji, and Q. Quan, "Design of simultaneous high-Q and high-sensitivity photonic crystal refractive index sensors," *J. Opt. Soc. Amer. B*, vol. 30, no. 8, pp. 2027–2031, 2013.
[37] D. Yang *et al.*, "High sensitivity and high Q-factor nanoslotted parallel quadrabeam photonic crystal cavity for real-time and label-free sensing," *Appl. Phys. Lett.* vol. 105, 2014, Art. no. 063118.
[38] D. Yang, H. Tian, and Y. Ji, "High-Q and high-sensitivity width-modulated photonic crystal single nanobeam air-mode cavity for refractive index sensing," *Appl. Opt.*, vol. 54, no. 1, pp. 1–5, 2015.
[39] D. Yang, H. Tian, and Y. Ji, "Nanoscale photonic crystal sensor arrays on monolithic substrates using side-coupled resonant cavity arrays," *Opt. Exp.*, vol. 19, no. 21, pp. 20023–20034, 2011.
[40] R. D. Peterson, B. T. Cunningham, and J. Andrade, "A photonic crystal biosensor assay for ferritin utilizing iron-oxide nano particles," *Biosens. Bioelectron.*, vol. 56, pp. 320–327, 2014.
[41] S. Hachuda *et al.*, "Selective detection of sub-atto-molar Streptavidin in 1013-fold impure sample using photonic crystal nanolaser sensors," *Opt. Exp.*, vol. 21, pp. 12815–12821, 2013.

[42] M. Loncar, A. Scherer, and Y. Qiu, "Photonic crystal cavity laser sources for chemical detection," *Appl. Phys. Lett.*, vol. 82, pp. 4648–4651, 2003.
[43] E. Chow, A. Grot, I. W. Mirkarimi, M. Sigalas, and G. Girolami, "Ultracompact bio-chemical sensor built with two-dimensional photonic crystal microcavity," *Opt. Lett.*, vol. 29, pp. 1093–1095, 2004.
[44] N. Skivesen, A. Tetu, M. Kristensen, J. Kjems, L. Frandsen, and P. Borel, "Photonic-crystal waveguide biosensor," *Opt. Exp.*, vol. 15, pp. 3169–3176, 2007.
[45] M. Lee and P. Fauchet, "Two-dimensional silicon photonic crystal based biosensing platform for protein detection," *Opt. Exp.*, vol. 15, pp. 4530–4535, 2007.
[46] A. Di Falco, L. OFaolain, and T. F. Krauss, "Chemical sensing in slotted photonic crystal heterostructure cavities," *Appl. Phys. Lett.*, vol. 94, 2009, Art. no. 063503.
[47] T. Lu, Y. Hsiao, W. Ho, and P. Lee, "High-index sensitivity of surface mode in photonic crystal hetero-slab-edge microcavity," *Opt. Lett.*, vol. 35, 2010, Art. no. 1452.
[48] W. Lai, S. Chakravarty, Y. Zou, and R. T. Chen, "Silicon nano-membrane based photonic crystal microcavities for high sensitivity bio-sensing," *Opt. Lett.*, vol. 37, pp. 1208–1210, 2012.
[49] T. Xu, N. Zhu, M. Y.-C. Xu, L. Wosinski, J. S. Aitchison, and H. E. Ruda, "Pillar-array based optical sensor," *Opt. Exp.*, vol. 18, pp. 5420–5425, 2010.
[50] Q. Quan and Y. Zhang, "Lab-on-a-Tip (LOT): Where nanotechnology can revolutionize fibre optics," *Nanobiomedicine*, vol. 2, pp. 1–5, 2015.
[51] G. Shambat *et al.*, "A photonic crystal cavity-optical fiber tip nanoparticle sensor for biomedical applications," *Appl. Phys. Lett.*, vol. 100, 2012, Art. no. 213702.
[52] G. Shambat *et al.*, "Single-Cell photonic nanocavity probes," *Nano Lett.*, vol. 13, no. 11, pp. 4999–5005, 2013.
[53] B. Park *et al.*, "Double-layer silicon photonic crystal fiber-tip temperature sensors," *IEEE Photon. Technol. Lett.*, vol. 26, no. 9, pp. 900–903, May 2014.
[54] C. H. Bui, J. Zheng, S. Hoch, L. Lee, J. G. E. Harris, and C. Wong, "High-reflectivity, high-Q micromechanical membranes via guided resonances for enhanced optomechanical coupling" *Appl. Phys. Lett.*, vol. 100, 2012, Art. no. 021110.
[55] A. E. Miroshnichenko, S. Flach, and Y. S. Kivshar, "Fano resonances in nanoscale structures," *Rev. Modern Phys.* vol. 82, pp. 2257–2298, 2010.
[56] P. Fan, Z. Yu, S. Fan, and M. Brongersma, "Optical Fano resonance of an individual semiconductor nanostructure," *Nature Mater.*, vol. 13, pp. 471–475, 2014
[57] W. Ding, B. L. Yanchuk, and C. W. Qiu, "Ultrahigh-contrast-ratio silicon Fano diode," *Phys. Rev. A*, vol. 85, 2012, Art. no. 025806.
[58] W. Zhao, X. Leng, and Y. Jiang, "Fano resonance in all-dielectric binary nanodisk array realizing optical filter with efficient linewidth tuning," *Opt. Exp.*, vol. 23, no. 5, pp. 6858–6866, 2015.
[59] Y. Shuai *et al.*, "Double-layer Fano resonance photonic crystal filters," *Opt. Exp.*, vol. 21, no. 21, pp. 24582–24589, 2013.
[60] L. Chen, Z. Qiang, H. Yang, H. Pang, Z. Ma, and W. Zhou, "Polarization and angular dependent transmissions on transferred nanomembrane Fano filters," *Opt. Exp.*, vol. 17, no. 10, pp. 8396–8406, 2009.
[61] J. Liu, M. Schulmerich, R. Bhargava, and B. Cunningham, "Sculpting narrowband Fano resonances inherent in the large-area mid-infrared photonic crystal microresonators for spectroscopic imaging," *Opt. Exp.*, vol. 22, no. 15, pp. 18142–18158, 2014.
[62] X. Piao, S. Yu, and N. Park, "Control of Fano asymmetry in plasmon induced transparency and its application to plasmonic waveguide modulator," *Opt. Exp.*, vol. 20, no. 17, pp. 18994–18999, 2012.
[63] M. Rybin, D. Filonov, P. Belov, Y. Kivshar, and M. Limonov, "Switching from visibility to invisibility via fano resonances: Theory and experiment," *Sci. Rep.*, vol. 5, 2015, Art. no. 8774.
[64] L. Stern, M. Grajower, and U. Levy, "Fano resonances and all-optical switching in a resonantly coupled plasmonic-atomic system," *Nature Commun.*, vol. 5, 2014, Art. no. 4865.
[65] Y. Yu *et al.*, "Fano resonance control in a photonic crystal structure and its application to ultrafast switching," *Appl. Phys. Lett.*, vol. 105, 2014, Art. no. 061117.
[66] K. Nozaki, A. Shinya, S. Matsuo, T. Sato, E. Kuramochi, and M. Notomi, "Ultralow-energy and high-contrast all-optical switch involving Fano resonance based on coupled photonic crystal nanocavities," *Opt. Exp.*, vol. 21, no. 10, pp. 11877–11888, 2013.
[67] Y. Zhang, Y. Zhen, O. Neumann, J. Day, P. Nordlander, and N. Halas, "Coherent anti-Stokes raman scattering with single-molecule sensitivity using a plasmonic Fano resonance," *Nature Commun.*, vol. 5, 2014, Art. no. 4424.
[68] C. Wu *et al.*, "Fano-resonant asymmetric metamaterials for ultrasensitive spectroscopy and identification of molecular monolayers," *Nature Mater.*, vol. 11, pp. 69–75, 2012.
[69] K. Lee, J. Huang, J. Chang, S. Wu, and P. Wei, "Ultrasensitive biosensors using enhanced Fano resonances in capped gold nanoslit arrays," *Sci. Rep.*, vol. 5, 2015, Art. no. 8547.
[70] W. Ren, Y. Dai, H. Cai, H. Ding, N. Pan, and X. Wang, "Tailoring the coupling between localized and propagating surface plasmons: Realizing Fano-like interference and high-performance sensor," *Opt. Exp.*, vol. 21, no. 8, pp. 10251–10258, 2013.
[71] S. Wang *et al.*, "Optofluidic double-layer fano resonance photonic crystal slab liquid sensors," in *Proc. Conf. Lasers Electro-Opt.*, 2015, paper STu1F.6.
[72] J. Zhang, X. Zhang, X. Su, Y. Lu, S. Feng, and L. Wang, "Sensitivity enhancement through overlapping simultaneously excited Fano resonance modes of metallic-photonic-crystal sensors," *Opt. Exp.*, vol. 22, no. 3, pp. 3296–3305, 2014.
[73] M. Beheiry, V. Liu, S. Fan, and O. Levi, "Sensitivity enhancement in photonic crystal slab biosensors," *Opt. Exp.*, vol. 18, no. 22, pp. 22702–22714, 2010.
[74] L. Shi, P. Pottier, Y. Peter, and M. Skorobogatiy, "Guided-mode resonance photonic crystal slab sensors based on bead monolayer geometry,"*Opt. Exp.*, vol. 16, no. 22, pp. 17962–17971, 2008.
[75] W. Suh, M. Yanik, O. Solgaard, and S. Fan, "Displacement-sensitive photonic crystal structures based on guided resonance in photonic crystal slabs," *Appl. Phys. Lett.*, vol. 82, 2003, Art. no. 1999.

[76] N. Huang, L. Martinez, and M. Povinelli, "Tuning the transmission lineshape of a photonic crystal slab guided-resonance mode by polarization control," *Opt. Exp.*, vol. 21, no. 18, pp. 20675–20682, 2013.
[77] J. Li and S. Zouhdi, "Fano resonance filtering characteristic of high-resistivity silicon photonic crystal slab in terahertz region," *IEEE Photon. Technol. Lett.*, vol. 24, no. 8, pp. 625–627, Apr. 2012.
[78] C. Grillet *et al.*, "Characterization and modeling of Fano resonances in chalcogenide photonic crystal membranes," *Opt. Exp.*, vol. 14, no. 1, pp. 369–376, 2006.
[79] A. Rosenberg *et al.*, "Guided resonances in asymmetrical GaN photonic crystal slabs observed in the visible spectrum," *Opt. Exp.*, vol. 13, no. 17, pp. 6564–6571, 2005.
[80] J. Lee *et al.*, "Observation and differentiation of unique high-Q optical resonances near zero wave vector in macroscopic photonic crystal slabs," *Phys. Rev. Lett.*, vol. 109, 2012, Art. no. 067401.
[81] S. Fan and J. D. Joannopoulos, "Analysis of guided resonances in photonic crystal slabs," *Phys. Rev. B*, vol. 65, 2002, Art. no. 235112.
[82] S. Lee, J. Park, and C. Kee, "Fano resonance of self-collimated beams in two-dimensional photonic crystals," *Opt. Exp.*, vol. 22, no. 23, pp. 28954–28965, 2014.
[83] M. Galli, S. Portalupi, M. Belotti, L. Andreani, L. O'Faolain, and T. Krauss, "Light scattering and Fano resonances in high-Q photonic crystal Nanocavities," *Appl. Phys. Lett.*, vol. 94, 2009, Art. no. 071101.
[84] T. Prasad, V. Colvin, and D. Mittleman, "Dependence of guided resonances on the structural parameters of terahertz photonic crystal slabs," *J. Opt. Soc. Amer. B*, vol. 25, no. 4, pp. 633–644, 2010.
[85] X. Chew, G. Zhou, H. Yu, and F. Chau, "Fano resonance phenomenon utilizing photonic crystal rods for tunable filter applications," in *Proc. Int. Conf. Opt. MEMs Nanophoton.*, 2008, pp. 142–143.
[86] L. J. Sherry, S. Chang, G. C. Schatz, and R. P. Van Duyne, "Local-ized surface plasmon resonance spectroscopy of single silver nanocubes," *Nano Lett.*, vol. 5, pp. 2034–2038, 2005.
[87] J. Deng *et al.*, "Modeling and experimental investigations of Fano resonances in free-standing LiNbO3 photonic crystal slabs," *Opt. Exp.*, vol. 21, no. 3, pp. 3243–3252, 2013.